Progress In Electromagnetics Research B, Vol. 40, 305–324, 2012

A FEASIBILITY STUDY ON MICROWAVE IMAGING FOR BRAIN STROKE MONITORING

R. Scapaticci^{1,2}, L. Di Donato^{2}, I. Catapano^{1}, and L. Crocco^{1,*}

[1]CNR-IREA, National Research Council of Italy, Institute for Electromagnetic Sensing of the Environment, Via Diocleziano 328, Napoli 80124, Italy

[2]DIMET, University Mediterranea of Reggio Calabria, Via Graziella, Loc. Feo di Vito, Reggio Calabria 89100, Italy

Abstract—The adoption of microwave imaging as a tool for non-invasive monitoring of brain stroke has recently gained increasing attention. In this respect, the paper aims at providing a twofold contribution. First, we introduce a simple design tool to devise guidelines to properly set the working frequency as well as to choose the optimum matching medium needed to facilitate the penetration of the probing wave into the head. Second, we propose an imaging strategy based on a modified formulation of the linear sampling method, which allows a quasi real time monitoring of the disease's evolution. The accuracy of the design guidelines and performance of the imaging strategy are assessed through numerical examples dealing with 2D anthropomorphic phantoms.

1. INTRODUCTION

A stroke occurs when blood circulation into the brain fails due to a blocked or burst blood vessel and can cause serious diseases or even death if not timely detected. According to the American Heart/Stroke Association, cerebral stroke is the third cause of death in the United States [1].

Currently, the main clinical imaging tools used to detect and diagnose brain strokes are computerized tomography (CT) and/or magnetic resonance imaging (MRI). These techniques are largely assessed and provide an effective means to identify the stroke's location

---

Received 20 February 2012, Accepted 18 April 2012, Scheduled 2 May 2012

* Corresponding author: Lorenzo Crocco (crocco.l@irea.cnr.it).

and kind. However, they are not cost effective, their operation is time consuming and the involved instrumentations are not portable. As such, they are not suitable to be used in the continuous monitoring of stroke's evolution. Moreover, CT uses ionizing radiations and is therefore harmful for the safety of the patient. These circumstances motivate the interest for new technologies that can integrate the currently available ones to improve the overall effectiveness of the diagnosis.

In this respect, several research groups are investigating the possibility to use microwave tomography (MWT) for brain imaging. This trend relies on three main observations. The first one is the evidence that ischemic tissues show, in the microwave band, different electric properties with respect to healthy tissues [2, 3]. The second one is that microwaves are particularly suitable to perform a continuous monitoring, since they are not harmful for the patient, being non-ionizing radiations. Third, microwave technology allows to design portable and cost-effective devices.

Accordingly, in the recent years, several contributions, concerned with both MWT exposure devices and imaging strategies have been proposed in the literature [4–11]. In particular, as far as the imaging task is concerned, these contributions aim at achieving a map of the dielectric properties of the inspected brain tissues through the solution of an inverse scattering problem [12]. Since this problem is non-linear and ill-posed, suitable inversion methods, such as the Newton Kantorovich [4] or the Contrast Source Inversion method [10], have been adopted. However, these inversion methods are prone to the occurrence of false solutions [13], that is, erroneous outcomes of the imaging process. As such, to overcome this drawback, they need to process data measured at different frequencies, which in turn requires to cope with the non trivial broadband characterization of the electric properties of inspected tissues. Moreover, they are computationally expensive and therefore not viable for real-time monitoring.

With respect to such a framework, this paper aims at providing a twofold contribution.

First, we give some criteria useful to move towards the design of an optimized apparatus for brain imaging. In this respect, we provide hints to address the choice of the matching medium needed to improve the coupling between the probing wave and the inspected tissues, as well as the most convenient working frequency range. Although the overall design involves many other parameters (such as transmitting and receiving units, antennas and so on), the choice of the frequency and the matching medium is, in some sense, a preliminary step in the system's design, because it fixes the main features of the working environment.

Second, since it is extremely important to follow the changes in the stroked area, in order to timely treat its uncontrolled or unexpected growth, we propose an imaging strategy in which microwaves cooperate with the well assessed and currently available diagnostics methods for an effective time lapse monitoring of brain stroke. In particular, by relying on the aforementioned synergy, we assume that the brain's structures are known (e.g., from CT or MR images) and describe a method in which MWT is in charge of tracking and imaging the stroke's evolution.

To perform the required task, we take into account that the pursued goal is to estimate, almost in real time, the size and the shape of the stroked area, while it is not necessary to provide the quantitative value of its permittivity and conductivity. Taking these considerations into account, we consider an imaging approach based on the linear sampling method (LSM) [14], as this method is able to provide an image of the shape of an unknown target in a reliable and not computationally demanding way. In particular, the proposed inversion approach is based on a modified formulation of the LSM [15], specifically designed to image small targets located in a known, possibly complex, environment. By paralleling with the problem at hand, the stroke corresponds to the searched target and the anatomical brain structures is the known surrounding scenario.

The paper is structured as follows. Section 2 describes the adopted strategy to devise the design guidelines for the imaging device and addresses numerical proofs to check their validity. The description of the imaging strategy is given in Section 3. In Section 4, some numerical simulations are presented to asses the performance of the imaging strategy. Finally, in Section 5 conclusions are given. Note that both the guidelines' validation and the imaging examples are carried out against 2D scenario based on MRI derived anthropomorphic phantoms. Although being a simplified scenario, such a test bed is suitable to assess the proposed design tool and to provide a preliminary demonstration of the feasibility of the proposed microwave imaging method.

2. ON THE DESIGN OF THE IMAGING SYSTEM

2.1. Achieving Some Design Guidelines

The aim of this section is to derive some guidelines concerning the design of a microwave imaging system for brain stroke monitoring. To this end, let us start from the following two premises.

(i) A first key feature to successfully pursue the imaging task is the maximization of the amount of incident power that penetrates into the brain tissues. As a matter of fact, this ensures that some meaningful backscattered signal from the head's interior will arise, thus making the imaging possible.

(ii) A second key feature is to ensure the conditions needed by the processing strategy to provide images having the highest possible spatial resolution, in order to detect even small anomalies. In this respect, we recall that the spatial resolution achievable by MWT is dictated by the wavelength in the matching medium, i.e., the medium where the probed region and the transmitting/receiving antennas are located [16].

According to these observations, a crucial role in the design of a MWT system is played by the choice of the working frequency as well as that of the matching medium, such to accomplish both these goals.

In order to give some guidelines to address the choice of these parameters, which are, to some extent, degrees of freedom in the system's design, one would need tools that are both easy to use and have a general validity. This means that these tools should rely on simple models while providing the required insight.

A tool of this kind has been introduced in the framework of breast cancer imaging [17], wherein to study the wave-breast interaction as a function of the working frequency and the matching medium, a simple 1D model, consisting of a sequence of planar layers having the extent and the properties of typical breast tissues, has been adopted. Notably, the effectiveness of the guidelines resulting from such a simple model has been successfully verified against 2D and 3D anthropomorphic breast phantoms [17, 18]. The adoption of such a simple model was based on the observation that the probing wavelength has to be small as compared to the breast's dimension, in order to allow detectability of small tumors and tissue details.

We can take advantage of a similar tool also in the present framework. As matter of fact, similar conditions hold in brain stroke monitoring, since the extent of the damaged area is expected to be much smaller than the head.

According to these reasonings, we model the head by means of a sequence of five planar layers having different dielectric features and length. The first layer is the skin, whose thickness is assumed to be 4 mm. The second and the third layers are the fat (4 mm) and the cortex bone (7 mm), respectively. The fourth layer accounts for the cerebrospinal fluid (CSF) of thickness 3 mm. Finally, the brain region, that is the region in which we want to guarantee the maximum penetration of the incoming field, is modeled as a half space.

A convenient way to study such a structure is to exploit the transmission line (TL) formalism, which amounts to consider an equivalent transmission line in which each section corresponds to a tissue layer, as sketched in Fig. 1(b). In such a model, Z_{mm}, Z_s, Z_f, Z_b, Z_{csf}, Z_{br} denote the characteristic impedances of the matching medium, the skin, the fat, the bone, the CSF, and the brain, respectively. The characteristic impedance of the n-th section is $Z_n = \sqrt{\mu_0/\varepsilon_0\varepsilon_n}$, where ε_n is the complex permittivity of the corresponding tissue, and the length of each line section is chosen according to the thickness values given above.

To take into account the frequency dispersive behavior of biological tissues, their electric properties have been evaluated according to the single-pole Cole-Cole model:

$$\varepsilon(\omega) = \varepsilon'(\omega) - j\varepsilon''(\omega) = \varepsilon_\infty + \frac{\Delta\varepsilon}{1 + j\omega\tau^{1-\alpha}} + \frac{\sigma_i}{j\omega\varepsilon_0}. \tag{1}$$

In Eq. (1), ω is the angular frequency, ε_∞ the high frequency permittivity, $\Delta\varepsilon$ the magnitude of the dispersion, τ the relaxation time constant, α the parameter that allows for the broadening of the dispersion, and σ_i the static ionic conductivity. For each tissue, these

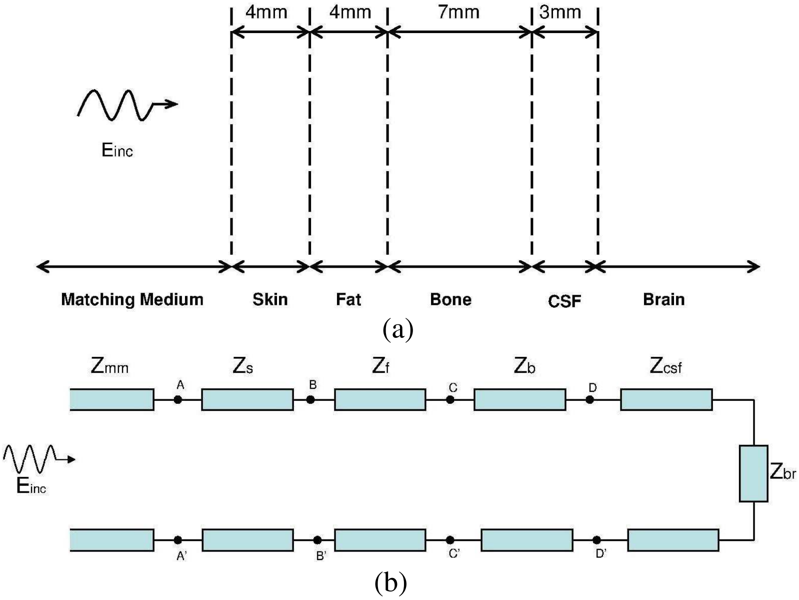

Figure 1. (a) Simplified layered model of human head, (b) corresponding transmission line model.

Table 1. Cole-Cole parameters of human head tissues.

Tissue	ε_∞	$\Delta\varepsilon$	τ	α	σ_i
Dry skin	4	32	7.23e-12	0	0.0002
Fat	2.5	3.0	7.96e-12	0.2	0.01
Bone	2.5	10	13.26e-12	0.2	0.02
Gray Matter	4	45	7.96e-12	0.1	0.02
White Matter	4	32	7.96e-12	0.1	0.02

parameters have been set according to the values given in [19] and reported in Table 1, but for the CSF, whose electric properties (i.e., $\varepsilon_{CSF} = 69.3$, $\sigma_{CSF} = 0.4\,\mathrm{S/m}$) are taken form [4], due to the non availability in the literature of Cole-Cole fitting parameters for this tissue. Note also that, as the brain is mainly composed by white and gray matter, the complex permittivity of the last layer has been set by averaging the complex permittivities of such tissues.

By taking advantage of the TL formalism and of the Cole-Cole modeling for tissues' frequency dispersion, we can calculate the total transmission coefficient T, which allows us to appraise the amount of incoming power that penetrates into the brain. This coefficient is defined as:

$$T = 1 - \Gamma, \tag{2}$$

wherein, Γ is the reflection coefficient at the section AA', see Fig. 1, corresponding to the interface between the matching medium and the skin, and defined as:

$$\Gamma = \frac{Z_{AA'} - Z_{mm}}{Z_{AA'} + Z_{mm}}, \tag{3}$$

wherein Z_{mm} is the characteristic impedance of the matching medium and $Z_{AA'}$ that of the head, as evaluated by means of the impedance transfer equation [20].

To analyze the role of the matching medium, as well as that of the working frequency, we have computed the transmission coefficient as function of frequency, in the microwave band of interest (100 MHz–10 GHz), and of the dielectric constant of the coupling medium, which is assumed to span from air to water $\varepsilon_{mm} \in [1 - 80]$.

Considering, at first, a lossless matching medium, we obtain the plot shown in Fig. 2(a), which reports the amplitude of the coefficient T. This plot suggests that a sort of "forbidden" band exists. As a matter of fact, in the 1.5–4 GHz range, $|T|$ is lower than 0.5 (in particular for low values of relative permittivity) and therefore the operating conditions appears not to be favorable for our purposes.

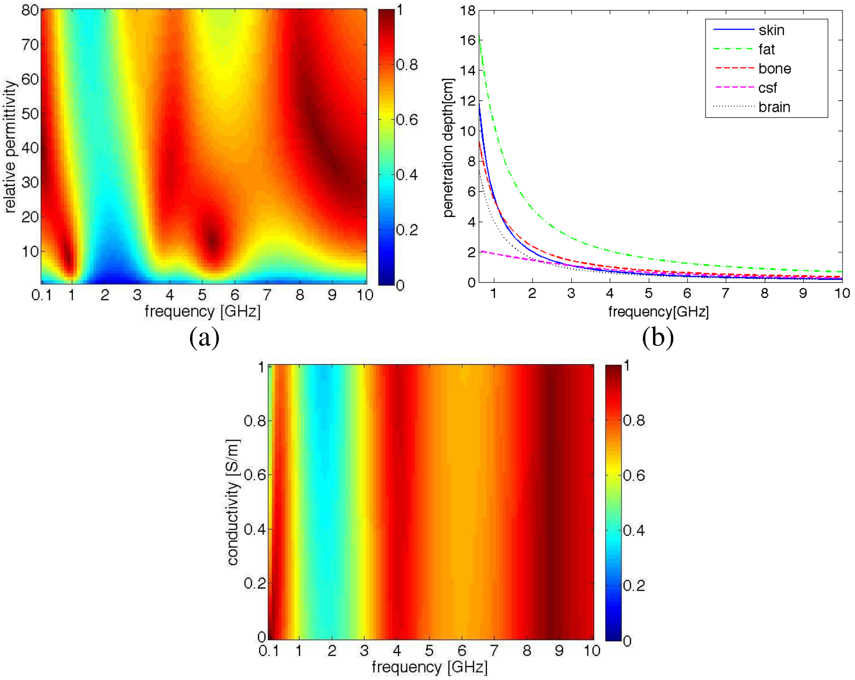

(a) (b)

(c)

Figure 2. (a) The transmission coefficient as a function of frequency and dielectric constant of the lossless matching medium, (b) skin depth for human head tissues, (c) the transmission coefficient as a function of frequency and conductivity of the matching medium, for $\varepsilon_{mm} = 40$.

Interestingly, the forbidden band is almost independent of the coupling medium. A possible, although qualitative, explanation of its occurrence can be given observing that a strong difference exists between the dielectric properties of cortex bone and fat layers and those of the CSF and that the overall electric length of these low permittivities layers (at frequencies belonging to the "forbidden" band) is such to create a strong mismatch. This ansatz is corroborated by the results of the numerical simulations shown in the next subsection.

On the other hand, considering working frequencies higher than 4 GHz is possible but not convenient, due to the low penetration depth in the inspected tissues, as shown by the skin depth behaviour depicted in Fig. 2(b). Similarly, lower frequencies (below 600 MHz) can also be adopted as they bring high values of $|T|$, but for a relative permittivity grater than 20. However, this frequency band does not allow to reach the required spatial resolution for the imaging task, also for a very dense matching medium. Taking these considerations into account, we can identify the 0.6–1.5 GHz range as the most convenient frequency band.

With respect to such a frequency range, from Fig. 2(a) we can assume that the dielectric constant of the matching medium can be almost arbitrarily chosen as belonging to the range 10–40. While this ensures a good flexibility, the achievable spatial resolution is, as recalled, dictated by the background's medium wavelength [16]. Therefore, this suggests that a matching medium having a relative permittivity as large as possible would be preferable.

Last but not least, to take into account the fact that a realistic matching medium will have a certain amount of losses, we have analyzed the behavior of $|T|$ for a fixed value of the real part of the medium's dielectric permittivity, i.e., $\varepsilon_{mm} = 40$, while varying its conductivity. Fig. 2(c) shows that, for a fixed frequency, the medium's conductivity does not meaningfully affect the transmission coefficient values.

2.2. Validation of the Retrieved Parameters Design against Realistic Scenarios

The aim of this section is to discuss the effectiveness of the guidelines given in Section 2.1 by investigating how they affect the penetration of the field inside the brain. To this end, we consider an anthropomorphic head model derived from the repository available in [21]. This phantom has been originated from a MR image consisting of 256 × 256 × 128 cells with dimensions of $1.1\,mm \times 1.1\,mm \times 1.4\,mm$, associating to each pixel of the image the complex permittivity value of the corresponding tissue [22].

In particular, we consider the transverse slice $n_z = 63$ of the original 3D-phantom (see Figs. 3(a), (b)) by adopting the original spatial discretization both to preserve the morphological complexity of the anatomic structures and to accurately solve the electromagnetic forward scattering problem [23]. On the other hand, we reduce the size of the original image to achieve a final image with 200 × 200 pixels, by removing part of the pixels belonging to the air/background region.

With respect to the phantom described above, we have then simulated the scattering experiments using a full wave forward simulator based on the method of moments (MoM). In particular, we have considered a set of incident fields radiated by 32 line sources evenly spaced on a circumference with radius $R = 18\,\mathrm{cm}$, and, for each of them, the currents induced inside the head have been computed.

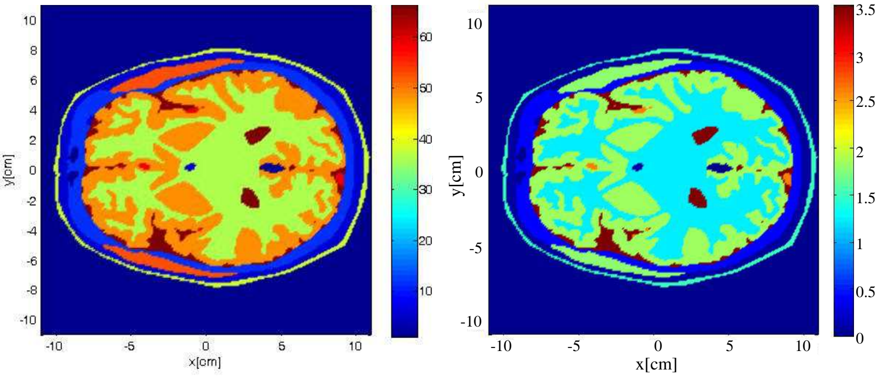

(a) (b)

Figure 3. Spatial map of the electric properties of Zubal phantom, slice 63, at $f = 2.5\,\mathrm{GHz}$. (a) Relative permittivity, (b) effective conductivity [S/m].

Three different situations in terms of matching medium and working frequency have been analyzed to assess the validity of the TL model.

At first, the scattering phenomenon has been simulated at $f = 1\,\mathrm{GHz}$ with a matching medium having permittivity $\varepsilon_{mm} = 40$ and conductivity $\sigma_{mm} = 0.01\,\mathrm{S/m}$. Note this value takes into account those possibly achievable with realistic media [24]. According to the guidelines given in the previous sub-section, this choice represents a sort of "best case" condition. Then, we have considered a working frequency belonging to the forbidden band by simulating the scattering experiment at $f = 2.5\,\mathrm{GHz}$. At this frequency we have considered two different media having $\varepsilon_{mm} = 40$, $\sigma_{mm} = 0.01\,\mathrm{S/m}$ and $\varepsilon_{mm} = 6.5$, $\sigma_{mm} = 0.0016\,\mathrm{S/m}$, respectively. In particular, in the second case, the dielectric properties of the matching medium have been chosen in order to get a comparison against the expected "best case" in terms of the same background wavenumber, i.e., the head has always the same electric size in terms of the probing wavelength.

Figures 4(a)–(c) show the normalized sum of the induced currents magnitude over all the illumination directions. As we can see, the overall induced current varies considerably in the three cases. In particular, as far as the expected "best case" is concerned, the magnitude of the induced currents in the brain region is indeed larger than the other cases. On the other hand, when the frequency is set at 2.5 GHz and the matching medium parameters are $\varepsilon_{mm} = 40$, $\sigma_{mm} = 0.01\,\mathrm{S/m}$, we can observe that the overall induced current remains

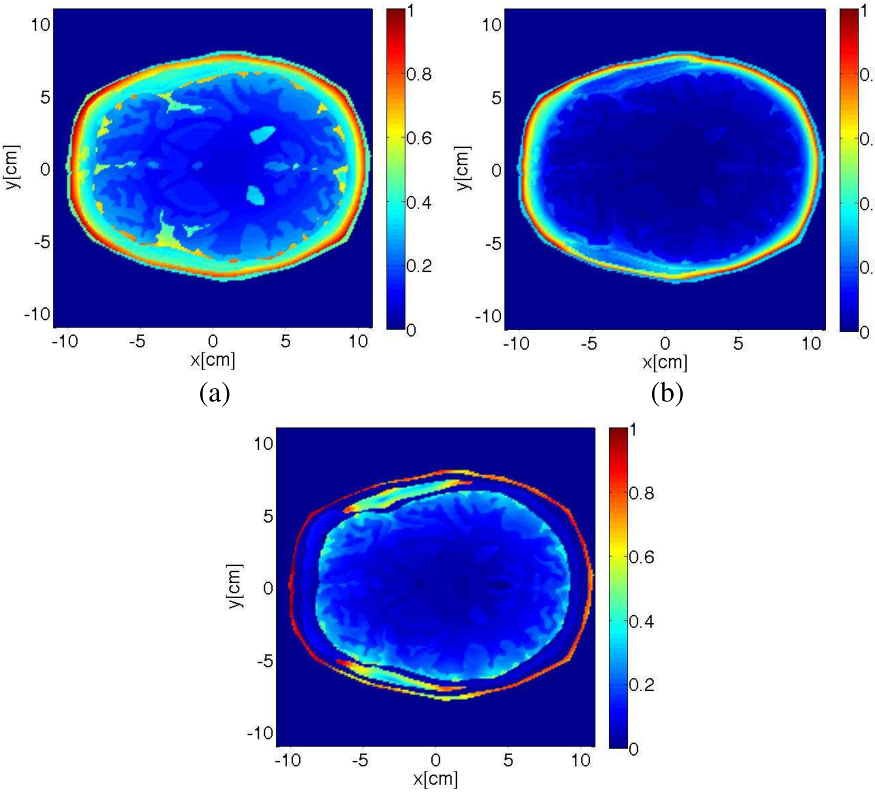

(a) (b)

(c)

Figure 4. Validation of the proposed guidelines. Normalized induced currents for different working frequencies and matching media. (a) $f = 1\,\mathrm{GHz}$, $\varepsilon_{mm} = 40$, $\sigma_{mm} = 0.01\,\mathrm{S/m}$, (b) $f = 2.5\,\mathrm{GHz}$, $\varepsilon_{mm} = 40$, $\sigma_{mm} = 0.01\,\mathrm{S/m}$, (c) $f = 2.5\,\mathrm{GHz}$, $\varepsilon_{mm} = 6.5$, $\sigma_{mm} = 0.0016\,\mathrm{S/m}$.

confined in the first layers of the head and a stronger attenuation of the field can be noticed in the brain region, see Fig. 4(b). Finally, when the medium parameters are $\varepsilon_{mm} = 6.5$, $\sigma_{mm} = 0.0016\,\mathrm{S/m}$ and the freqeuncy is $2.5\,\mathrm{GHz}$, the spatial distribution of the induced currents reveals that reflections and mismatch are predominant through tissues' layers, due to the presence of the fat and bone layers. This numerical evidence supports the hypothesis given in Section 2.1 about the occurrence of the "forbidden band".

To conclude this section, we observe that the given numerical analysis suggests the suitability of the TL model to address the choice of both the frequency and the electric properties of the matching medium. In this respect, it is worth to point out that all previous studies concerned with MWT for brain imaging [4–10] consider working frequencies lying in the 0.5–2 GHz range. Therefore, on the one hand, the proposed modeling tool allows to provide an explanation of this, otherwise simply empirical, choice and, on the other hand, these papers provide an indirect validation of the guidelines we are proposing.

3. STROKE IMAGING VIA MODIFIED LINEAR SAMPLING

The imaging approach we consider is a modified version of the LSM proposed in [15], which takes advantage of the knowledge of the brain structures arising from other diagnostic techniques, such as CT or MRI. In the following, we first recall the basics of the original LSM formulation, then we illustrate its modified formulation to deal with the case at hand.

Let $\mathbf{E}_s$ denote the $N \times N$ scattered field data matrix collected using an array made of N antennas operated under a multiview-multistatic measurement configuration. In this arrangement, each antenna works both as transmitter and receiver, and when an antenna is transmitting the backscattered signal is recorded at all N antennas. Hence, the generic element of $\mathbf{E}_s$ is the electric field $E_s^n(\mathbf{r}_m)$ scattered by the unknown target and measured at the receiving position $\mathbf{r}_m$ when the n-th antenna is active.

Without requiring any approximation or assumption but for the above ones concerning the measurement arrangement, the LSM consists in partitioning the investigated domain Ω into an arbitrary grid of sampling points ($\mathbf{r}_p$) and in solving, for each of them, the following matrix equation [14]:

$$\mathbf{E}_s \mathbf{x}(\mathbf{r}_p) = \mathbf{G}(\mathbf{r}_m, \mathbf{r}_p), \tag{4}$$

wherein $\mathbf{x}(\mathbf{r}_p)$ is the N-dimensional unknown vector and $\mathbf{G}(\mathbf{r}_m, \mathbf{r}_p)$ the N-dimensional vector, whose elements are the values of the Green's function as applied in the sampling point $\mathbf{r}_p$ and evaluated at the N receivers position $\mathbf{r}_m \in \Gamma$. In 2D scalar case at hand, this Green's function corresponds to the Hankel function of zero-th order and second kind for the homogeneous background medium.

A stable solution of Eq. (4) can be achieved by exploiting the SVD of $\mathbf{E}_s$ and the Tikhonov regularization [12]. The L^2-norm of the regularized solution is claimed to assume large values when $\mathbf{r}_p$ is outside the support of the object and low values elsewhere [14]. Therefore one gets an estimate of the geometrical features of the unknown target by simply computing and plotting over Ω the LSM solution energy:

$$\Upsilon(\mathbf{r}_p) = \|\mathbf{x}(\mathbf{r}_p)\|^2 = \sum_{n=1}^{N} \left(\frac{\lambda_n}{\lambda_n^2 + \alpha^2}\right)^2 |\langle \mathbf{G}(\mathbf{r}_p), \mathbf{u_n}\rangle|^2, \tag{5}$$

wherein λ_n are the singular values of $\mathbf{E_s}$ and $\mathbf{u_n}$ its right-hand singular vectors [12]. In Eq. (5), α is the Tikhonov weighting coefficient chosen according to the criterion given in [15], which allows to fix it independently from the knowledge of the SNR and only once for all the sampling points.

While addressing the reader to [14, 25–27], for more details, let us here recall that Eq. (4) corresponds, for each sampling point, to the attempt of rearranging the measured scattered fields in such a way that their linear combination according to $\mathbf{x}$ matches, at the receving locations, the field radiated by an elementary source located in the sampling point $\mathbf{r}_p$. The physical analogy between the LSM and an electromagnetic focusing problem [25, 27] suggests that achieving such a linear combination is possible only in sampling points belonging to the scatterer's support. This allows to explain why the energy of the unknown function $\mathbf{x}$ assumes low values in the target's support and large values elsewhere.

However, when processing the fields scattered by the head tissues embedding the stroke using standard LSM, it is not possible to obtain information about the presence of the stroke, since the LSM solution will provide an image of the overall shape of the head.

To overcome this limitation, it is possible to tackle the stroke imaging problem via a modified version of the LSM [15]. As a matter of fact, we can exploit the knowledge about the electromagnetic features of the head tissues to formulate the imaging problem in a "differential" fashion, that is, as the search for a perturbation with respect to a known scenario.

Formally, this corresponds to solve an equation having the same structure as Eq. (4), in which the data matrix and the right hand side are changed according to this new framework. Such a modified equation reads:

$$\Delta\mathbf{E}_s \mathbf{y}(\mathbf{r}_p) = \widetilde{\mathbf{G}}(\mathbf{r}_m, \mathbf{r}_p), \tag{6}$$

where $\Delta\mathbf{E}_s$ is the difference between the measured data (i.e., in presence of the stroke) and the data computed by simulating the known"unperturbed" reference scenario (i.e., the healthy brain), and the right hand side $\widetilde{\mathbf{G}}$ now expresses the Green function of the inhomogeneous scenario, i.e., the field of an elementary source radiating in the healthy brain as evaluated at the receivers.

Given the formal analogy with the standard LSM equation, we can notice that Eq. (6) corresponds, for each sampling point, to the attempt of rearranging the "differential" data in such a way that their linear combination ruled by $\mathbf{y}$ matches, at the receiving locations, the field radiated by an elementary source located in the sampling point $\mathbf{r}_p$. Hence, we can foresee that the L^2 norm of solution $\mathbf{y}$ will assume large values when $\mathbf{r}_p$ is outside of areas exhibiting anomalous properties with respect to the healthy brain and low values elsewhere. To build the image resulting from the modified LSM, we adopt a compensated LSM indicator defined as:

$$\Delta\Upsilon(\mathbf{r}_p) = \frac{\|\mathbf{y}(\mathbf{r}_p)\|^2}{\left\|\tilde{\mathbf{G}}(\mathbf{r}_p)\right\|^2} = \frac{1}{\left\|\tilde{\mathbf{G}}(\mathbf{r}_p)\right\|^2} \sum_{n=1}^{N} \left(\frac{\lambda_n}{\lambda_n^2 + \alpha^2}\right)^2 \left|\left\langle \tilde{\mathbf{G}}(\mathbf{r}_p), \mathbf{u_n} \right\rangle\right|^2, \tag{7}$$

wherein λ_n and $\mathbf{u_n}$ are now related to the SVD of $\Delta\mathbf{E}_s$, while the Tikhonov coefficient α is still computed as in [15].

In (7) the energy of the solution $\mathbf{y}$ is divided by the squared norm of the right hand side of Eq. (6) in each sampling point. This allows to compensate the attenuation of the field, due to the different location of the sampling points with respect to the receivers. By referring the reader to [27] for more details, we point out only that such a normalization improves the readability of the imaging result when dealing with large domain with respect to the probing wavelength and highly lossy media such as human tissues.

As last comment it is worth to note that the modified LSM formulation requires to numerically compute the inhomogeneous background's Green function $\tilde{\mathbf{G}}$. To perform this task, taking into account that transmitters and receivers positions are the same, we can rely on Lorentz reciprocity. Accordingly, we solve the forward scattering problem for all N transmitters when they radiate in presence of the (healthy) brain, since the resulting total field corresponds to the required Green's function.

4. NUMERICAL EXAMPLES

In this section we address a numerical assessment to investigate the imaging capability of the proposed method for brain stoke monitoring. In this respect, we adopt two different slices of the 3-D phantom and for each of them, we consider two strokes of different dimension, in order to simulate two stages in the disease's evolution.

The imaged area is the same as the one considered in Section 2.2 and the same numerical MoM based forward solver has been adopted to generate the scattered field data and compute the inhomogeneous Green's function $\tilde{\mathbf{G}}$ (through reciprocity). In both cases, the stroke is modeled as an ellipsis-shaped anomaly with dielectric properties equal to $\varepsilon_s = 36$, $\sigma_s = 0.72\,\mathrm{S/m}$ [4, 5]. In the first case (A) the stroke has major semi-axis $a = 1\,\mathrm{cm}$ and minor semi-axis $b = 0.5\,\mathrm{cm}$, while in the second case (B) the semi-axes are $a = 2\,\mathrm{cm}$ and $b = 1\,\mathrm{cm}$, respectively.

Taking into account the results given in Section 2, the head is probed at 1 GHz, by means of an array made of $N = 32$ filamentary sources located on circle of radius $R = 18\,\mathrm{cm}$, embedded in a matching medium having electric properties $\varepsilon_{mm} = 40$ and $\sigma_{mm} = 0.01\,\mathrm{S/m}$. Note that 1 GHz is also the frequency at which the electric contrast between healthy tissues and stroked area is maximum [2–4].

For each phantom, the performance of the proposed imaging method has been first assessed considering noise-free data, as this allows to appraise the "best result" that can be obtained by the method. Note that, since completely different equations are used to simulate the data and to form the image, such an idealized processing is not an inverse crime [12], but rather an actual assessment of the procedure in the most favorable working conditions. Moreover, in order to assess the capability of the approach in more realistic conditions, we have also repeated the same examples considering the unavoidable presence of uncertainties on the reference scenario and noise on data. In particular, we have corrupted the simulated data by an additive gaussian noise with $SNR = 60\,\mathrm{dB}$ and we have introduced a zero average ±2.5% random variability of the electromagnetic properties of the tissues in the phantoms, to simulate the natural variability of actual tissues. Note that the average values of the electromagnetic properties of the tissues have been instead used to evaluate the Green's function $\tilde{\mathbf{G}}$.

In the first example, we have considered the slice $n_z = 45$ of the original MR phantom with a stroked area centered at $x = -2\,\mathrm{cm}$ and $y = -2.5\,\mathrm{cm}$. First, we show the image obtained using the modified LSM indicator (7) in ideal conditions. The achieved reconstructions, shown in Figs. 5(c)–(d), reveal that the location, the dimension and the shape of the stroke are correctly estimated by the method for both the smaller and the larger strokes. The result in presence of uncertainties on the scenario and noise on data are shown in Figs. 5(e)–(f), from which one can appraise that also when such unavoidable errors are present, the modified LSM is still capable to provide satisfactory results, thus suggesting the possibility of monitoring the growth of the stroke. Obviously, increasing the non-ideality will lead to worse images.

As a second example, we have considered the phantom derived by another slice ($n_z = 63$) of the Zubal phantom (see Figs. 6(a), (b)).

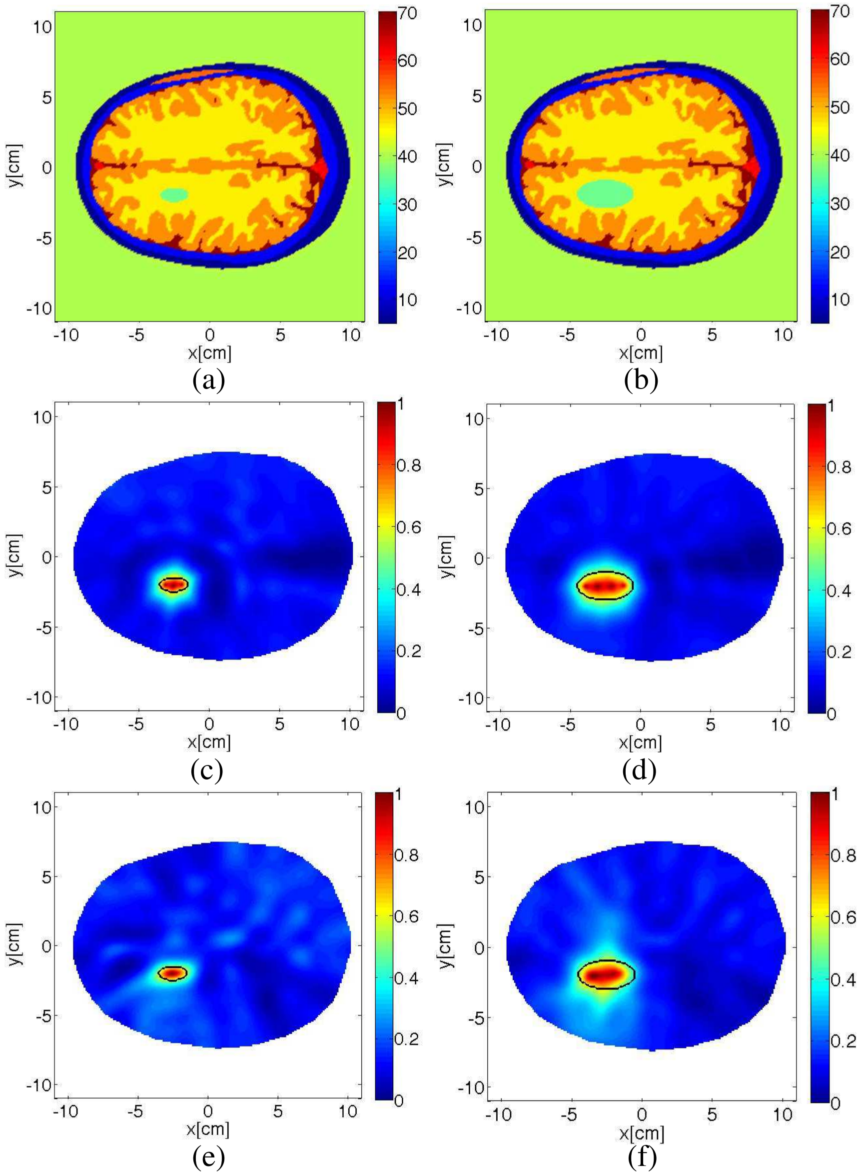

Figure 5. Validation of the proposed imaging approach. Reference scenario: (a) with the small stroke, (b) with the large stroke. MWT image in ideal conditions: (c) small stroke, (d) large stroke. (e) MWT image in realistic conditions: (f) small stroke, (e) large stroke.

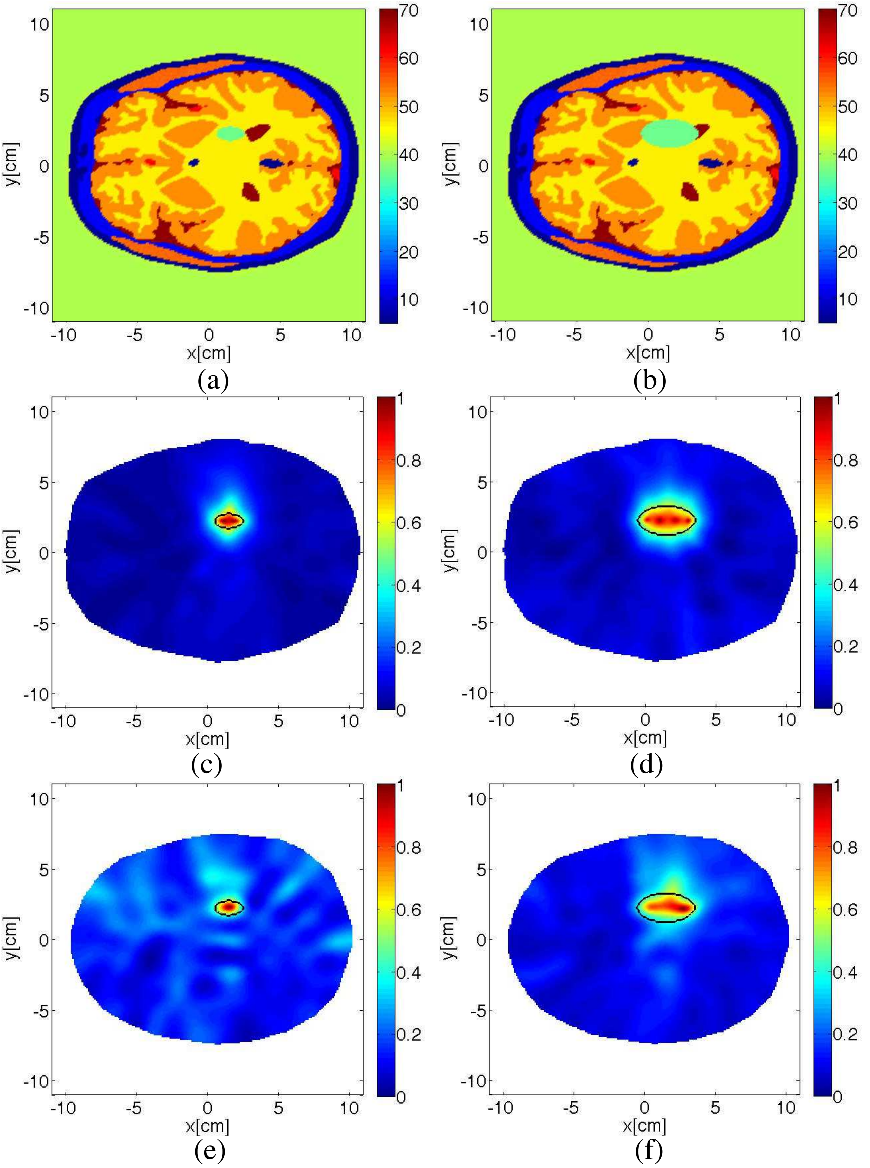

Figure 6. Validation of the proposed imaging approach. Reference scenario: (a) with the small stroke, (b) with the large stroke. MWT image in ideal conditions: (c) small stroke, (d) large stroke. (e) MWT image in realistic conditions: (f) small stroke, (e) large stroke.

Note that in this case both the dimension and the anatomical brain structures are much more complex as compared to the previous case. The simulated ellipsis-shaped strokes have the same electric properties and dimension of the the previous example, but they are centered at $x = 2.2\,\text{cm}$ and $y = 1.5\,\text{cm}$. Also in this case, see Figs. 6(c)–(f), the proposed method is able to obtain an accurate result in ideal conditions as well as in presence of uncertainties, although, as expected, the image deteriorates in the second case.

5. CONCLUSIONS

In the framework of microwave brain imaging, the paper has addressed two issues.

First of all, some criteria to set the working frequency range and the choice of the optimum matching medium have been provided by taking advantage of a simplified head model based on the transmission line formalism. Notably, this study not only explains the empirical choices commonly followed in literature to set these two basic design parameters, but also provides a more general tool to address the design for brain stroke monitoring based on microwave imaging. As a second contribution, a microwave imaging approach has been proposed to perform an effective monitoring of brain stroke's evolution. Notably, such an approach has been thought to act in a cooperative fashion with other diagnostics tools usually adopted in the diagnosis of strokes, but not suitable for their continuous monitoring.

The performed analysis, although being preliminary, suggests that the proposed method is worth to be considered in the framework of the emerging microwave based technologies for stroke brain imaging. Moreover, its outcomes give a further *a posteriori* proof of the validity of the guidelines devised by means of the proposed simple design tool.

In this respect, the achieved results against 2D anthropomorphic head phantoms motivate the ongoing studies aimed at extending the proposed tool in the more realistic 3D case, wherein the well assessed effectiveness of the LSM to tackle the full vectorial imaging problem [28, 29] will be exploited. Also, we will consider the assessment of the proposed imaging strategy against other kind of uncertainties, such as for instance inaccurate positioning of the measurement probes.

REFERENCES

1. Rosamon, W., et al., "Heart disease and stroke statistics — 2007 update: A report from the American heart association statistics

committee and stroke statistics subcommittee," *Circulation*, Vol. 115, e69–e171, 2007.

2. Semenov, S. Y., R. H. Svenson, and G. P. Tatsis, "Microwave spectroscopy of myocardial ischemia and infarction. 1. Experimental study," *Ann. Biomed. Eng.*, Vol. 28, 48–54, 2000.
3. Semenov, S. Y., et al., "Dielectrical spectroscopy of canine myocardium during acute ischemia and hypoxia at frequency spectrum from 100 kHz to 6 GHz," *IEEE Trans. Med. Imaging*, Vol. 21, 547–550, 1994.
4. Semenov, S. Y. and D. R. Corfield, "Microwave tomography for brain imaging: Feasibility assessment for stroke detection," *Int. J. Antennas Propag.*, Vol. 2008, Article ID 254830, 8 pages, 2008.
5. Ireland, D. and M. Bialkowski, "Feasibility study on microwave stroke detection using a realistic phantom and the FDTD method," *Proc. of Asia Pacific Microwave Conference*, Singapore, 2010.
6. Ireland, D. and M. Bialkowski, "Microwave head imaging for stroke detection," *Progress In Electromagnetics Research M*, Vol. 21, 163–175, 2011
7. Mesri, H. Y., M. K. Najafabadi, and T. McKelvey, "A multidimensional signal processing approach for classification of microwave measurements with application to stroke type diagnosis," *33rd Annual International Conference of the IEEE EMBS*, Boston, 2011.
8. Fhager, A. and M. Persson, "A microwave measurement system for stroke detection," *Antennas and Propagation Conference (LAPC)*, Loughborough, UK, Nov. 14–15, 2011.
9. Sultana, E., A. Khwaja, K. Mansetaa, Y. Mallalaha, Q. Zhang, L. Najafizadehc, A. Gandjbakhche, K. Pourrezad, and A. S. Daryoush, "Comparison of tethered and untethered helmet mounted fNIR systems for TBI application," *IEEE Wireless and Microwave Technology Conference*, 2011.
10. Gilmore, C., A. Abubakar, W. Hu, T. M. Habashy, and P. M. van den Berg, "Microwave biomedical data inversion using the finite-difference contrast source inversion method," *IEEE Trans. Antenn. Propag.*, Vol. 57, 1528–1538, 2009.
11. Mohammed, B. J., A. M. Abbosh, D. Ireland, and M. E. Bialkowski, "Compact wideband antenna for microwave imaging of brain stroke," *Progress In Electromagnetics Research C*, Vol. 27, 27–39, 2012.

12. Bertero, M. and P. Boccacci, "Introduction to inverse problems in imaging," *Inst. Phys.*, Bristol, UK, 1998.
13. Isernia, T., V. Pascazio, and R. Pierri, "On the local minima in a tomographic imaging technique," *IEEE Trans. Geosci. Remote Sens.*, Vol. 39, 1596–1607, 2001.
14. Cakoni, F. and D. Colton, *Qualitative Methods in Inverse Scattering Theory*, Springer-Verlag, Berlin Heidelberg, 2006.
15. Catapano, I. and L. Crocco, "An imaging method for concealed targets," *IEEE Trans. Geosci. Remote Sens.*, Vol. 47, 1301–1309, 2009.
16. Slaney, M., A. C. Kak, and L. E. Larsen, "Limitations of imaging with first-order diffraction tomography," *IEEE Trans. Microwave Theory Tech.*, Vol. 32, 860–874, 1984.
17. Catapano, I., L. Di Donato, L. Crocco, O. M. Bucci, A. F. Morabito, T. Isernia, and R. Massa, "On quantitative microwave tomography of female breast," *Progress In Electromagnetics Research*, Vol. 97, 75–93, 2009.
18. Catapano, I., L. Crocco, L. Di Donato, G. Angiulli, T. Isernia, A. F. Morabito, S. Tringali, O. M. Bucci, and R. Massa, "Guidelines for effective microwave breast imaging: An accurate numerical assessment against 3D anthropomorphic phantoms," *Proceeding EUCAP 2010 — European Conference on Antennas & Propagation*, Barcelona, Spain, Apr. 12–16, 2009.
19. Gabriel, S., R. W. Lau, and C. Gabriel, "Dielectric properties of biological tissue: III. Parametric models for the dielectric spectrum of tissues," *Phys. Med. Biol.*, Vol. 41, 2271–2293, 1996.
20. Balanis, C. A., *Advanced Engineering Electromagnetics*, John Wileys and Sons, 1989.
21. Zubal, I. G., C. R. Harrell, E. O. Smith, Z. Rattner, G. Gindi, and P. B. Hoffer, "Computerized three-dimensional segmented human anatomy," *Med. Phys.*, Vol. 21, No. 2, 299–302, 1994.
22. "Dielectric properties of body tissues in the frequency range 10 Hz–100 GHz," http://niremf.ifac.cnr.it/tissprop.
23. Richmond, J., "Scattering by a dielectric cylinder of arbitrary cross section shape," *IEEE Trans. Antenn. Propag.*, Vol. 13, No. 13, 334–341, 1965.
24. Romeo, S., L. Di Donato, O. M. Bucci, I. Catapano, L. Crocco, M. R. Scarfí, and R. Massa, "Dielectric characterization study of liquid based materials for mimicking breast tissues," *Microwave Opt. Tech. Lett.*, Vol. 53, 1276–1280, 2011

25. Catapano, I., L. Crocco, and T. Isernia, "On simple methods for shape reconstruction of unknown scatterers," *IEEE Trans. Antenn. Propag.*, Vol. 55, 1431–1436, 2007.
26. Catapano, I., L. Crocco, and T. Isernia, "Linear sampling method: Physical interpretation and guidelines for a successful application," *PIERS Online*, Vol. 4, No. 2, 291–295, 2008.
27. Catapano, I., L. Crocco, and T. Isernia, "Sampling methods for shape reconstruction of 3D buried targets," *IEEE Trans. Geosci. Remote Sens.*, Vol. 46, 3265–3273, 2008.
28. Colton, D., K. Giebermann, and P. Monk, "A regularized sampling method for solving three dimensional inverses scattering problems," *SIAM J. Sci. Comput.*, Vol. 21, 2316–2330, 2000.
29. Catapano, I., L. Crocco, M. D'Urso, and T. Isernia, "3D microwave imaging via preliminary support reconstruction: Testing on the Fresnel 2008 database," *Inverse Probl.*, Vol. 25, 024002, 2009.